photonics

MDPI

Article

A Compact Dual-Axis Homodyne Grating Interferometer Using a Wollaston-Prism-Based Quadrant Detection Module

Dunbo Song [1,2], Di Chang [1,2,*] and Jiubin Tan [1,2]

[1] Center of Ultra-Precision Optoelectronic Instrument Engineering, Harbin Institute of Technology, Harbin 150080, China; 25b901027@stu.hit.edu.cn (D.S.); jbtan@hit.edu.cn (J.T.)
[2] Key Lab of Ultra-Precision Intelligent Instrumentation, Ministry of Industry and Information Technology, Harbin Institute of Technology, Harbin 150080, China
* Correspondence: di.chang@hit.edu.cn

Abstract

A compact dual-axis homodyne grating interferometer with an integrated detection module based on Wollaston prisms and quadrant photodetectors is developed for displacement measurement in space-constrained precision motion systems. Rotating the upstream non-polarizing beam splitter by 45° about the incident optical axis adjusts the spatial arrangement of two parallel beams so that the four spots formed by each Wollaston prism are centered on the four photosensitive quadrants of the corresponding detector. This arrangement adapts the integrated detection module to dual-axis grating interferometry. The prototype measures 49.2 mm × 72.5 mm × 35 mm. In the separate-axis measurement experiments using two phasemeters, the 3σ values of the displacement fluctuations along the x- and z-axes were 6.06 nm and 8.10 nm, respectively, over 10 s stationary windows.

Keywords: homodyne grating interferometer; dual-axis displacement measurement; Wollaston prism; quadrant photodetector; integrated detection module

1. Introduction

Multi-degree-of-freedom precision displacement measurement plays a critical role in advanced instruments and equipment, including precision motion stages, machine tools, and lithography systems [1–5]. In a dual-stage lithography system, one wafer stage undergoes exposure while the other is measured by the metrology system. Arranging multiple sensing channels around a moving stage for six-degree-of-freedom measurement constrains the space available for each reading head [5,6]. Compact reading heads facilitate this arrangement while leaving space for the stage structure, actuators, and optical paths. Grating interferometers provide precision displacement feedback for motion stages, machine tools, and lithography systems [7–9]; their short free-space optical paths reduce sensitivity to fluctuations in the refractive index of air [10–13]. Homodyne grating interferometers use a single-frequency laser source and obtain quadrature signals through beam splitting, phase shifting, and multichannel detection [14–18]. Extending homodyne detection to two displacement axes also requires compact integration of the receiving optics for both interferometric channels [6,19–23].

Previous studies have explored the miniaturization and dual-axis measurement capabilities of homodyne grating interferometers [24,25]. Cheng and Fan assembled a single-axis grating interferometer within a 40 mm × 40 mm footprint by bonding miniature optical elements [26]. Kimura et al. used measurement and reference gratings to construct a dual-axis encoder head measuring approximately 50 mm × 50 mm × 30 mm [27]. Guan et al.

Check for updates

Received: 11 October 2026
Revised: 29 October 2026
Accepted: 22 November 2026
Published: 26 November 2026

Copyright: © 2026 by the authors. Licensee MDPI, Basel, Switzerland. This article is an open access article distributed under the terms and conditions of the Creative Commons Attribution (CC BY) license.

demonstrated a two-dimensional homodyne encoder using mirror-symmetric modules [28]. Table 1 summarizes representative homodyne grating interferometers in terms of their measurement axes, head dimensions, optical integration approaches, and reported performance. These configurations highlight the importance of integrating multichannel beam-splitting and detection optics when developing a compact reading head for both in-plane and out-of-plane displacement measurement [29–31].

Table 1. Dimensions, integration approaches, and reported performance of representative grating interferometers.

Study	Axes	Head Dimensions (mm)	Optical Integration	Reported Performance
Cheng and Fan (2011) [26]	x	40 × 40 (footprint)	Bonded miniature optics; one diffraction-phase measurement channel	Repeatability <15 nm ($\pm 2\sigma$) over 15 mm
Kimura et al. (2010) [27]	x, z	≈50 × 50 × 30	Scale and reference gratings integrated in a compact head	Sub-nanometer displacement resolution on both axes
Lu et al. (2016) [32]	x, z	Not miniaturized	Transmission scanning grating and reflective scale grating; grating and Michelson interferometry	Experimental dual-axis displacement measurement
Lin et al. (2017) [21]	x, y, z	130 × 130 × 68	Planar scale grating, reference grating, and diffracted-beam receiving optics	Resolution: 100 nm along x/y; 4 nm along z
This work	x, z	49.2 × 72.5 × 35	Two Wollaston prisms and two quadrant photodetectors acquire eight signals; two phasemeters reconstruct two displacement components	Residual 3σ over 100 μm: 146.20/159.35 nm; stationary 3σ over 10 s: 6.06/8.10 nm

An integrated receiving module based on a Wollaston prism (WP) and a quadrant photodetector (QPD) offers an approach to reducing the size of the detection optics in a homodyne interferometer. The WP performs polarization beam splitting [33–35], while the QPD receives different beams with its independent photosensitive quadrants, facilitating the compact integration of a multichannel detection architecture. Applying this arrangement to two diffraction channels requires both polarization mixing and spatial separation. Each reference–measurement beam pair must generate complementary interference signals, and the four output spots must fall on separate detector quadrants. If the prism orientation does not match the incident beam arrangement, the resulting tilted spot pattern reduces utilization of the photosensitive area and may extend beyond its boundaries.

In this study, a compact dual-axis homodyne grating interferometer incorporating a WP–QPD integrated detection module is developed. By rotating the upstream non-polarizing beam splitter by 45° about the incident optical axis, the two parallel beams are spatially arranged so that the four spots produced by each Wollaston prism are centered on the corresponding detector quadrants. The displacement equations are established under symmetric Littrow incidence, and a prototype reading head measuring 49.2 mm × 72.5 mm × 35 mm is constructed. Single-phasemeter separate-axis experiments demonstrate displacement measurement over a 100 μm stroke along both the in-plane x-axis and the out-of-plane z-axis, with displacement residuals relative to capacitive-sensor references of 184.27 nm and 157.81 nm (3σ), respectively. Repeatability and static stability are also evaluated, with short-term displacement fluctuations of 7.19 nm and 6.93 nm (3σ) within selected 20 s stationary windows. Two QPDs acquire the eight signals required for dual-phase readout, and two phasemeters reconstruct displacement from the phase sum and difference. Using two phasemeters, the residual 3σ values relative to the capacitive-sensor reference over a 100 μm stroke were 146.20 nm and 159.35 nm along the x- and z-axes, respectively. The corresponding stroke-deviation 3σ values were 430.35 nm and 217.21 nm, while the stationary displacement fluctuations over 10 s were 6.06 nm and 8.10 nm (3σ),

respectively. These results support the feasibility of integrating WP–QPD detection into a compact dual-axis homodyne grating interferometer.

2. Optical Configuration and Measurement Principle

2.1. Optical Configuration

The proposed dual-axis homodyne grating interferometer is shown in Figure 1. The in-plane direction perpendicular to the grating lines is defined as the *x*-axis, while the surface normal of the grating is defined as the *z*-axis. The interferometer consists of a single-frequency laser source, measurement optics, and an integrated quadrant detection module. The two interferometric paths carry combined phase information associated with the in-plane and out-of-plane displacements, from which the grating displacements along the *x*- and *z*-axes are obtained through phase detection and demodulation.

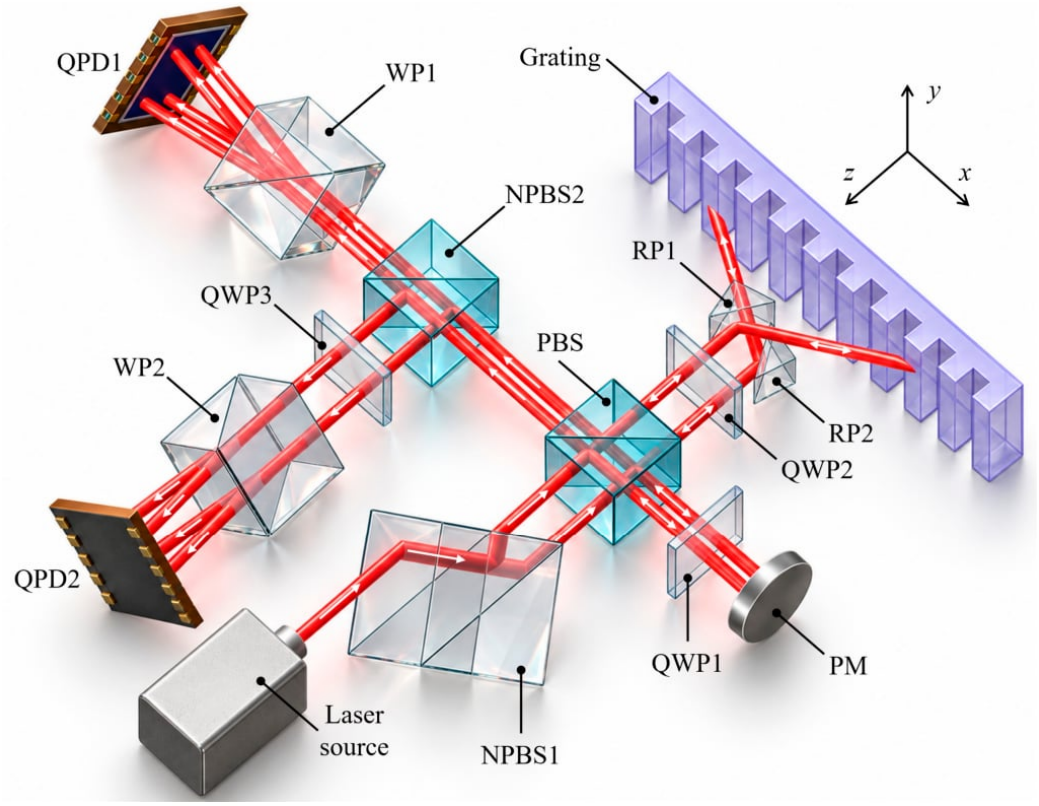

Figure 1. Optical configuration of the dual-axis homodyne grating interferometer. The in-plane *x*-axis and out-of-plane *z*-axis are defined relative to the grating. NPBS: non-polarizing beam splitter; PBS: polarizing beam splitter; QWP: quarter-wave plate; WP: Wollaston prism; QPD: quadrant photodetector; RP: right-angle prism; PM: plane mirror.

The measurement optics comprise a non-polarizing beam splitter (NPBS1), a polarizing beam splitter (PBS), a reference plane mirror (PM), two quarter-wave plates (QWP1 and QWP2, with their fast axes oriented at 45°), two right-angle prisms (RP1 and RP2), and the measurement grating. NPBS1, rotated by 45° about the incident optical axis, splits the single-frequency laser beam emitted by the laser source into two parallel beams, which subsequently enter the PBS, where the s-polarized components are reflected to form the reference beams and the p-polarized components are transmitted to form the measurement beams. Each reference beam is reflected by the PM and passes through QWP1 twice, thereby converting its polarization state from s polarization to p polarization, after which it returns to and is transmitted by the PBS. The two measurement beams are redirected

by RP1 and RP2, respectively, and impinge on the grating at symmetric Littrow angles; each measurement beam undergoes one diffraction at the grating and retraces its incident path. After passing through QWP2 twice, each measurement beam is converted from p polarization to s polarization and is subsequently reflected by the PBS, where it is recombined with its corresponding reference beam. In each recombined beam, the reference and measurement beams are orthogonally polarized and subsequently enter the integrated quadrant detection module.

The integrated quadrant detection module consists of a non-polarizing beam splitter (NPBS2), a quarter-wave plate (QWP3), two Wollaston prisms (WP1 and WP2), and two quadrant photodetectors (QPD1 and QPD2). NPBS2 distributes the two recombined beams between two detection branches, with QWP3 placed in the branch leading to WP2. WP1 projects the reference and measurement polarization components onto its ±45° analysis axes, producing complementary cosine signals. In the second branch, the principal axes of QWP3 are parallel to the two orthogonal incident polarization directions, and the analysis axes of WP2 are oriented at ±45° to these directions. Thus, the principal axes of QWP3 are oriented at 45° to the analysis axes of WP2. The quarter-wave retardation produces sine signals after the beams pass through WP2. Each WP produces four output beams, which are received by the four photosensitive quadrants of its corresponding QPD. Each QPD receives two complementary outputs for each diffraction order; the four quadrature signals used to recover one phase are obtained from both QPDs.

2.2. Spatial Matching of the Integrated Quadrant Detection Module

To achieve miniaturization of the interferometer, a WP–QPD integrated detection module is employed for polarization beam splitting and multichannel photodetection. Without rotation of NPBS1, the direction separating the two parallel incident beams and the splitting direction of the WP produce the tilted four-spot arrangement shown in Figure 2a. Rotating NPBS1 by 45° about the incident optical axis makes these two directions perpendicular. The center-to-center separation of the incident beams then determines one dimension of the spot array, while the separation of the WP output beams determines the other, as shown in Figure 2b. Equal separations in the two directions produce a square array.

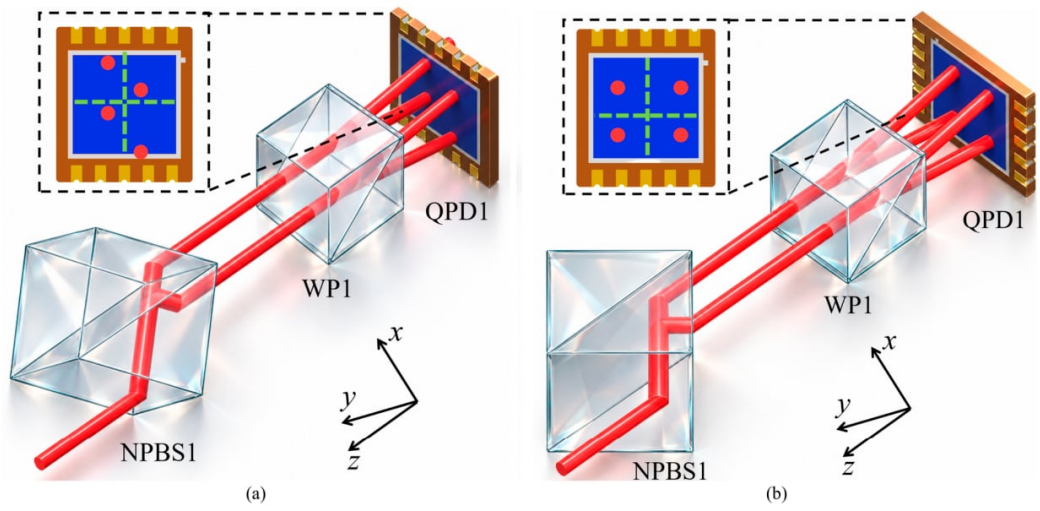

Figure 2. Spatial matching of the WP–QPD module: (**a**) spot distribution before rotation of NPBS1; (**b**) approximately square distribution obtained by rotating NPBS1 by 45° and adjusting the propagation distance.

The QPD used in this study is a Hamamatsu S5981, with a 10 mm × 10 mm photosensitive area divided into four quadrants by 30 μm-wide gaps.

As shown in Figure 3, the 15 mm NPBS provides a nominal beam separation of 5 mm at an incident height of 2.509 mm. For the WP10P Wollaston prism (Thorlabs), the calculated internal and external beam separation angles at 780 nm are approximately 11.05° and 19.30°, respectively. A nominal distance of 11.43 mm from the WP exit face to the QPD photosensitive surface produces a 5 mm beam separation in the orthogonal direction. The geometric relations and assembly tolerances are analyzed in Sections 4.1 and 4.2.

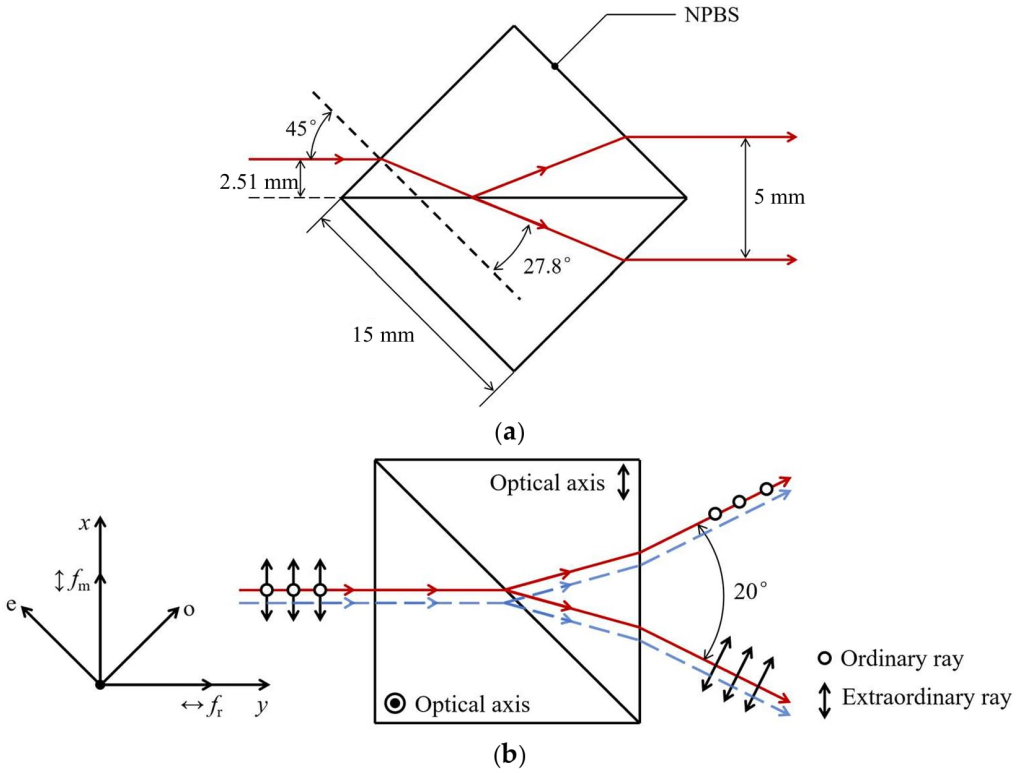

Figure 3. Beam-splitting geometry: (**a**) NPBS geometry producing a nominal beam separation of 5 mm for the incident beam; (**b**) WP polarization splitting, with the manufacturer's nominal 20° separation at 633 nm shown schematically. Red solid line and blue dash line are represent reference and measurement beam, respectively.

2.3. Measurement Principle

Let the frequency of the light source be f. Neglecting the initial phase, the optical field emitted by the single-frequency laser source can be expressed as:

$$E_0(t) = A_0 \cos(2\pi f t) \tag{1}$$

where A_0 is the electric-field amplitude. For each interferometric path, the reference and measurement fields can be expressed as:

$$\begin{cases} E_{r,M}(t) = A_{r,M} \cos\left[2\pi f t + \varphi_{r,M}\right] \\ E_{m,M}(t) = A_{m,M} \cos\left[2\pi f t + 2\pi \int_0^t \Delta f_M(\tau) \mathrm{d}\tau + \varphi_{m,M}\right] \end{cases} \tag{2}$$

where $A_{r,M}$ and $A_{m,M}$ are the amplitudes of the reference and measurement beams, respectively; $\varphi_{r,M}$ and $\varphi_{m,M}$ are their initial phases; M denotes the diffraction order, with $M = \pm 1$ considered in this study; and $\Delta f_M(t)$ is the Doppler frequency shift in the measurement beam induced by grating motion.

Let θ_{Lit} denote the angle of incidence with respect to the grating normal, d the grating period, and λ the laser wavelength in the propagation medium, which satisfy the first-order Littrow condition $2d\sin\theta_{\mathrm{Lit}} = \lambda$. Following the coordinate convention defined in

Figure 1, a positive displacement along the z-axis is defined to increase the phases of both interferometric paths in the same direction, whereas a positive displacement along the x-axis increases the phase of the +1-order diffracted beam and decreases that of the −1-order diffracted beam; accordingly, the Doppler frequency shift can be expressed as [29]:

$$\Delta f_M(t) = \frac{M}{d} v_x(t) + \frac{2\cos\theta_{\mathrm{Lit}}}{\lambda} v_z(t) = \frac{1}{d}[M v_x(t) + v_z(t)\cot\theta_{\mathrm{Lit}}] \tag{3}$$

where $v_x(t)$ and $v_z(t)$ are the grating velocities along the x- and z-axes, respectively.

After passing through the integrated quadrant detection module, the reference and measurement beams are superposed along the same polarization direction, and the optical intensity is obtained by taking the cycle average of the squared resultant electric field. After removing the DC component, the AC component of the cosine signal in the WP1 branch, $I_M(t)$, can be expressed as:

$$I_M(t) \propto \cos\left[2\pi \int_0^t \Delta f_M(\tau)\, \mathrm{d}\tau + \varphi_{0,M}\right] \tag{4}$$

where $\varphi_{0,M} = \varphi_{m,M} - \varphi_{r,M}$ is the initial phase difference. After normalizing the signal amplitudes, substituting Equation (3) into Equation (4) and taking $M = -1$ and $M = +1$, respectively, yields:

$$\begin{cases} I_{-1}(t) = \cos\left[\dfrac{2\pi}{d}\int_0^t (-v_x(\tau) + v_z(\tau)\cot\theta_{Lit})\mathrm{d}\tau + \varphi_{0,-1}\right] \\ I_{+1}(t) = \cos\left[\dfrac{2\pi}{d}\int_0^t (v_x(\tau) + v_z(\tau)\cot\theta_{Lit})\mathrm{d}\tau + \varphi_{0,+1}\right] \end{cases} \tag{5}$$

After phase demodulation by the phasemeter and subtraction of the initial phases, the phase changes in the two interference signals can be expressed as:

$$\begin{cases} \varphi_{-1} = \frac{2\pi}{d}(-\Delta x + \Delta z \cot\theta_{\mathrm{Lit}}) \\ \varphi_{+1} = \frac{2\pi}{d}(\Delta x + \Delta z \cot\theta_{\mathrm{Lit}}) \end{cases} \tag{6}$$

where Δx and Δz denote the relative displacements of the grating along the x- and z-axes, respectively. Taking the difference between the two phase changes eliminates the out-of-plane displacement term, while taking their sum eliminates the in-plane displacement term, yielding:

$$\begin{cases} \Delta x = \frac{d}{4\pi}(\varphi_{+1} - \varphi_{-1}) \\ \Delta z = \frac{d\tan\theta_{\mathrm{Lit}}}{4\pi}(\varphi_{+1} + \varphi_{-1}) \end{cases} \tag{7}$$

Equation (7) relates the two interferometric phases to the dual-axis displacements of the grating.

The four phase-shifted signals required for phase demodulation are generated as follows. Let $\Phi_M(t) = \varphi_{0,M} + \varphi_M(t)$ denote the total interference phase, where $\varphi_M(t)$ is the phase change defined in Equation (6). Omitting the common optical-frequency factor, the Jones vector of the recombined reference and measurement fields is

$$E_M = \left[A_{\mathrm{r},M}, A_{\mathrm{m},M} \mathrm{e}^{\mathrm{i}\Phi_M}\right]^{\mathrm{T}}. \tag{8}$$

Projecting the fields onto the two analysis axes of WP1 gives intensities proportional to $|A_{\mathrm{r},M} \pm A_{\mathrm{m},M}\exp(\mathrm{i}\Phi_M)|^2/2$. In the second branch, the fast and slow axes of QWP3 are aligned with the polarization directions of the incident reference and measurement beams, respectively, and are each at 45° to the ±45° analysis axes of WP2. In this polarization basis, the Jones matrix is $\mathrm{Q} = \mathrm{diag}(1, -\mathrm{i})$, giving intensities proportional to $|A_{\mathrm{r},M} \mp \mathrm{i}\, A_{\mathrm{m},M}\exp(\mathrm{i}\Phi_M)|^2/2$. The four detected signals can therefore be written as

$$I_{M,0} = B_{\mathrm{c},M} + A_{\mathrm{c},M}\cos\Phi_M, I_{M,180} = B_{\mathrm{c},M} - A_{\mathrm{c},M}\cos\Phi_M; \tag{9}$$

$$I_{M,90} = B_{s,M} + A_{s,M} \sin \Phi_M, I_{M,270} = B_{s,M} - A_{s,M} \sin \Phi_M. \quad (10)$$

Here, $B_{c,M}$ and $B_{s,M}$ are the mean intensities in the two receiving branches, and $A_{c,M}$ and $A_{s,M}$ are the interference signal amplitudes. The subscripts 0, 90, 180, and 270 indicate the nominal fringe-phase delays. QPD1 provides $I_{M,0}$ and $I_{M,180}$, while QPD2 provides $I_{M,90}$ and $I_{M,270}$. Subtracting the complementary signals gives the cosine and sine components:

$$C_M = I_{M,0} - I_{M,180}; S_M = I_{M,90} - I_{M,270}. \quad (11)$$

When the quadrature signal amplitudes are balanced, the fractional phase is atan2(S_M, C_M). Each phasemeter uses a field-programmable gate array (FPGA) to latch the sampled signals, track the integer fringe count, and calculate the fractional phase using the coordinate rotation digital computer (CORDIC) algorithm. Combining the integer count and fractional phase yields a continuous phase record. CORDIC-based programmable gain control [14] was enabled in the experimental phasemeters.

As shown in Figure 4, one four-input phasemeter processes the +1-order signals and the other processes the −1-order signals. The personal computer (PC) aligns the two phase records using their timestamps and subtracts their respective initial phases. The resulting phase changes are combined using Equation (7).

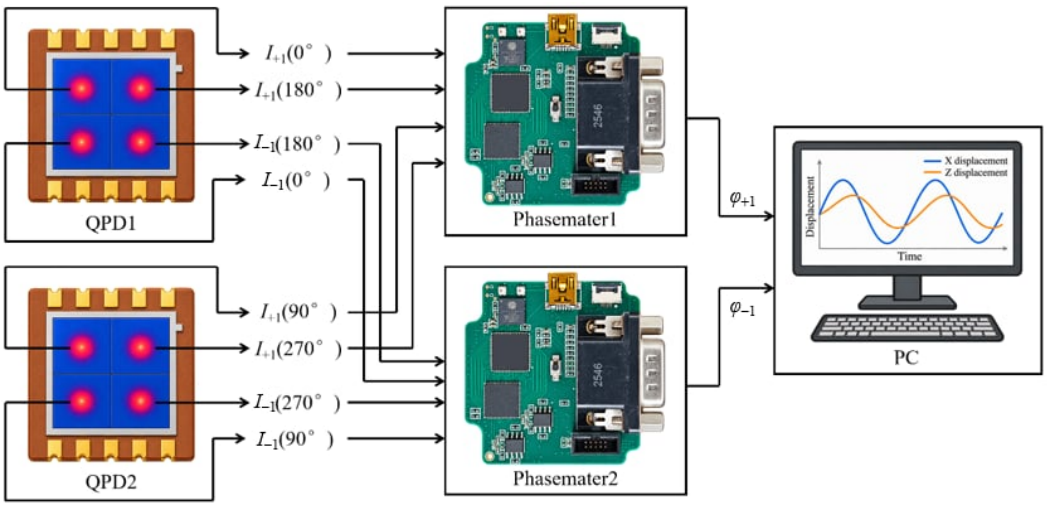

Figure 4. Dual-phase acquisition and displacement reconstruction. Signals corresponding to the same diffraction order are grouped across QPD1 and QPD2 and fed to one phasemeter. The personal computer (PC) aligns the two phase records using their timestamps and calculates the *x*- and *z*-axis displacements.

When the stage is driven along either nominal axis, this reconstruction also retains the displacement component in the other direction.

3. Experimental Setup and Results

3.1. Compact Prototype and Experimental Setup

The compact dual-axis homodyne grating interferometer reading head is shown in Figure 5. QWP1 and QWP2 are bonded to the PBS, PM is bonded to the PBS assembly, and QWP3 is bonded to NPBS2. The reading head has overall dimensions of 49.2 mm × 72.5 mm × 35 mm.

The experimental setup is shown in Figure 6. A TEC 500 semiconductor laser(Sacher Lasertechnik Group, Marburg, Germany) was used as the single-frequency laser source, with a central wavelength of 780 nm and an output power of up to 30 mW. A rotatable polarizing beam splitter was placed between the reading head and the laser to adjust

the polarization direction of the incident beam. The reading head was mounted on a three-axis adjustment stage to adjust its position relative to the measurement grating and thereby achieve optical alignment. A reflective grating with 1200 lines/mm was used as the measurement grating, corresponding to a nominal grating period of approximately 833.3 nm and a Littrow angle of 27.9°. The measurement grating was mounted, via an adapter, on a P-541.2CD two-axis piezoelectric positioning stage (Physik Instrumente, Karlsruhe, Germany). Stage motion is described in the x/z coordinate system defined with respect to the grating.

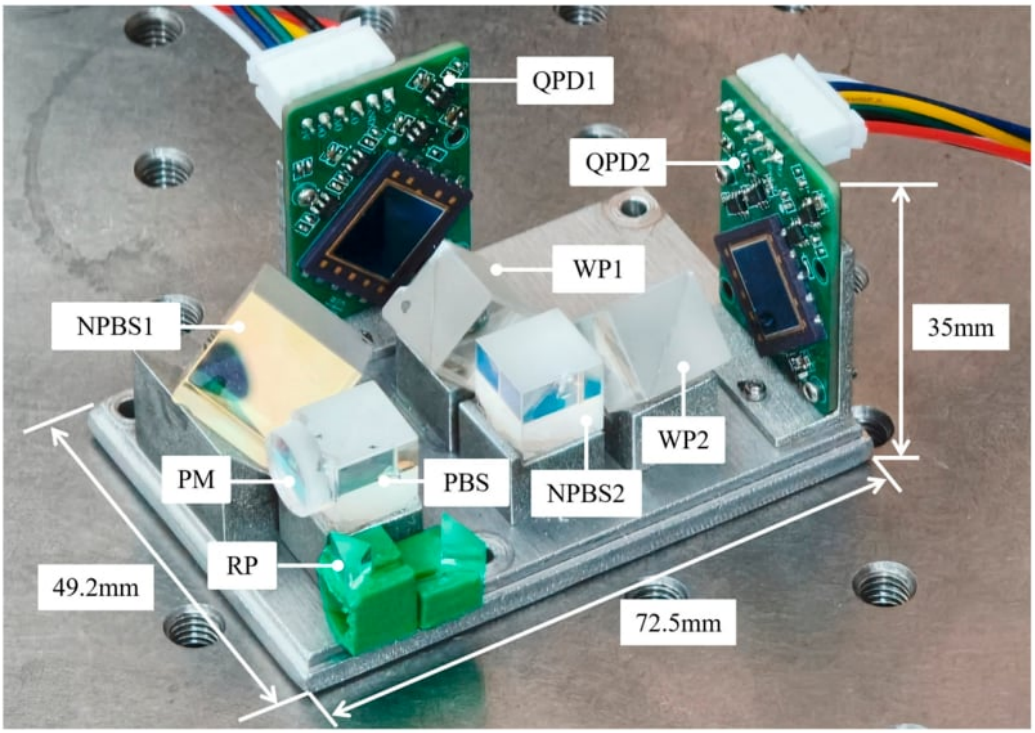

Figure 5. Compact reading head and its main optical components.

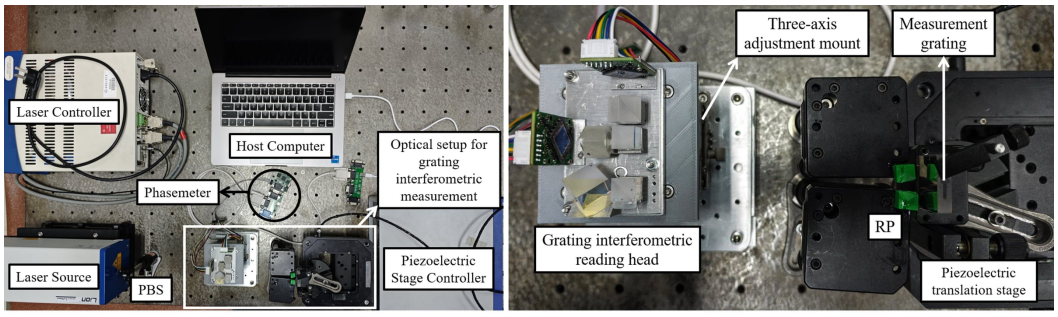

Figure 6. Experimental setup: (**a**) overall arrangement; (**b**) reading head, measurement grating, and piezoelectric positioning stage.

The piezoelectric positioning stage incorporates capacitive sensors, whose measurements were used as reference data. The manufacturer specifies a closed-loop travel range of 100 µm per axis, a typical linearity error of 0.03%, and a typical repeatability of less than 5 nm for the P-541.2CD positioning stage. The typical linearity specification corresponds to 30 nm over the 100 µm closed-loop range. The interferometer outputs are compared with the capacitive-sensor readings recorded in this setup.

The experiments used single-phasemeter separate-axis measurements and displacement reconstruction using two phasemeters. The FPGA processing clock operated at 28.8 MHz. The PC recorded displacement at 10 Hz. The interferometer and capacitive-sensor data were aligned using their timestamps, and no digital filtering was applied to the recorded displacement data. Linear-motion, repeated-stroke, and stationary experiments were performed with both readout configurations to evaluate agreement with the reference measurements, dispersion of stroke-amplitude deviations, and short-term displacement fluctuations, respectively.

3.2. Single-Phasemeter Separate-Axis Measurements

In the single-phasemeter experiments, the four inputs were quadrature signals for the same diffraction order obtained from the two QPDs. The positioning stage was driven separately along the x- and z-axes, and the measured phase changes were converted into displacement using the phase sensitivity of the corresponding axis.

3.2.1. Linear Displacement Measurements

Using PI digital motion-control software (PIMikroMove2.4.0.0), the piezoelectric positioning stage was driven separately along the x- and z-axes to perform uniform linear motion over a stroke of 100 μm. The measured displacement curves are shown in Figure 7. Let $D_{\mathrm{GI},j}$ and $D_{\mathrm{cap},j}$ denote the interferometer and capacitive-sensor displacements, respectively, where $j = x$ or z. The residual at the aligned time t_i is defined as

$$r_j(t_i) = D_{\mathrm{GI},j}(t_i) - D_{\mathrm{cap},j}(t_i). \tag{12}$$

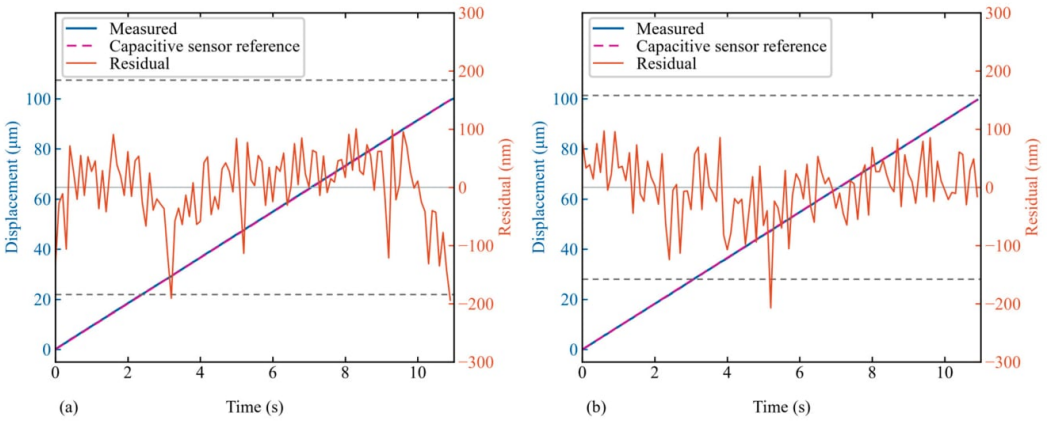

Figure 7. Linear-motion measurements over a 100 μm stroke using a single phasemeter: (**a**) x-axis; (**b**) z-axis. The blue and magenta curves show the interferometer and capacitive-sensor reference displacements, respectively. The orange-red curves show the residuals on the right-hand vertical axes. The gray dashed lines indicate $\pm 3\sigma$ of the residuals.

The maximum absolute deviations from the reference displacements along the x- and z-axes were 193.90 nm and 207.15 nm, respectively. The standard deviations of the displacement residuals were 61.42 nm and 52.60 nm, corresponding to 3σ values of 184.27 nm and 157.81 nm, respectively.

3.2.2. Repeated-Stroke Measurements

The piezoelectric positioning stage was driven separately along the x- and z-axes in a reciprocating triangular-wave motion with a peak-to-peak displacement of 100 μm, and the measurement results are shown in Figure 8. For the kth one-way stroke, the stroke

deviation is defined as the difference between the interferometer stroke amplitude $A_{\mathrm{GI},j,k}$ and the capacitive-sensor reference stroke amplitude $A_{\mathrm{cap},j,k}$,

$$e_{j,k} = A_{\mathrm{GI},j,k} - A_{\mathrm{cap},j,k}, (k = 1, \ldots, N), \tag{13}$$

where N is the number of one-way strokes in each record. Each single-phasemeter record contained 15 one-way strokes, as shown in Figure 8. The sample standard deviations of the stroke-amplitude deviations along the x- and z-axes are 136.28 nm and 98.86 nm, respectively, corresponding to 3σ values of 408.84 nm and 296.57 nm, which characterize the dispersion of the stroke-amplitude deviations over the repeated reciprocating motions.

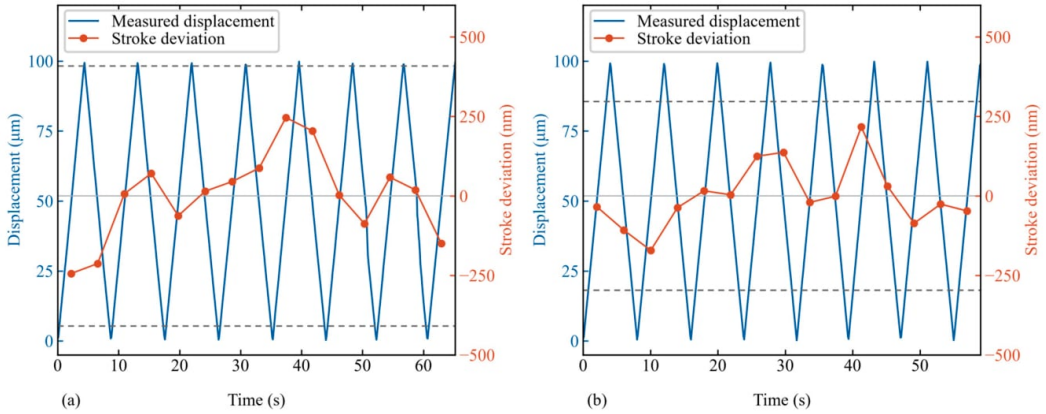

Figure 8. Repeated-stroke measurements using a single phasemeter: (**a**) x-axis; (**b**) z-axis. The blue curves show displacement on the left-hand vertical axes. The orange-red markers show the deviations of 15 stroke amplitudes from the capacitive-sensor reference values on the right-hand vertical axes. The gray solid and dashed lines indicate zero deviation and $\pm 3\sigma$, respectively.

3.2.3. Short-Term Stability

After the interferometer had stabilized, with the positioning stage held stationary, the interferometer outputs along the x- and z-axes were recorded separately. For each axis, the 20 s stationary window of the raw displacement data was selected for analysis. Figure 9 shows the displacement fluctuations within these selected windows. The blue and red curves correspond to the x- and z-axes, respectively, and the horizontal dashed lines indicate $\pm 3\sigma$. The sample standard deviations were 2.40 nm and 2.31 nm, corresponding to 3σ values of 7.19 nm and 6.93 nm, respectively. These values characterize short-term fluctuations within the selected windows. Table 2 summarizes the single-phasemeter measurement results.

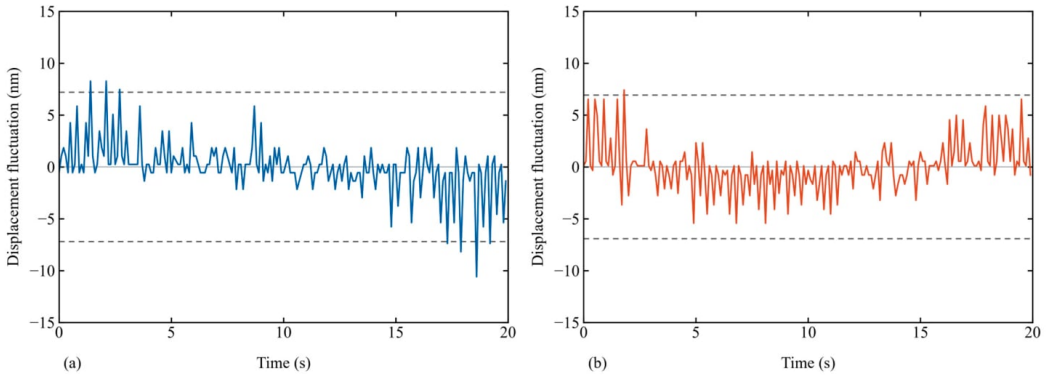

Figure 9. Displacement fluctuations within 20 s stationary windows using a single phasemeter: (**a**) x-axis; (**b**) z-axis. The gray dashed lines indicate $\pm 3\sigma$. The 3σ values are 7.19 nm and 6.93 nm for the x- and z-axes, respectively.

Table 2. Experimental results of the single-phasemeter separate-axis measurements.

Metric	*x*-Axis (nm)	*z*-Axis (nm)
Linear-motion residual, 3σ	184.27	157.81
Maximum absolute linear-motion residual	193.90	207.15
Stroke deviation, 3σ	408.84	296.57
Stationary displacement fluctuation, 3σ	7.19	6.93

3.3. Displacement Reconstruction Using Two Phasemeters

In the experiments using two phasemeters, the phasemeters processed the signals from the positive and negative first-order diffraction channels, respectively. Both diffraction phases were recorded during each experiment and combined using Equation (7) to reconstruct the *x*- and *z*-axis displacements.

3.3.1. Linear Displacement Measurements

The positioning stage performed linear motion over a nominal stroke of 100 μm along the *x*- and *z*-axes. The displacement reconstruction results obtained using two phasemeters are shown in Figure 10. The residuals relative to the capacitive-sensor reference were calculated using Equation (12). Their standard deviations were 48.73 nm and 53.12 nm for the *x*- and *z*-axes, corresponding to 3σ values of 146.20 nm and 159.35 nm, respectively. The maximum absolute residuals were 135.30 nm and 161.05 nm, respectively. In these records, the residuals relative to the capacitive-sensor reference exhibited similar dispersion along the two axes.

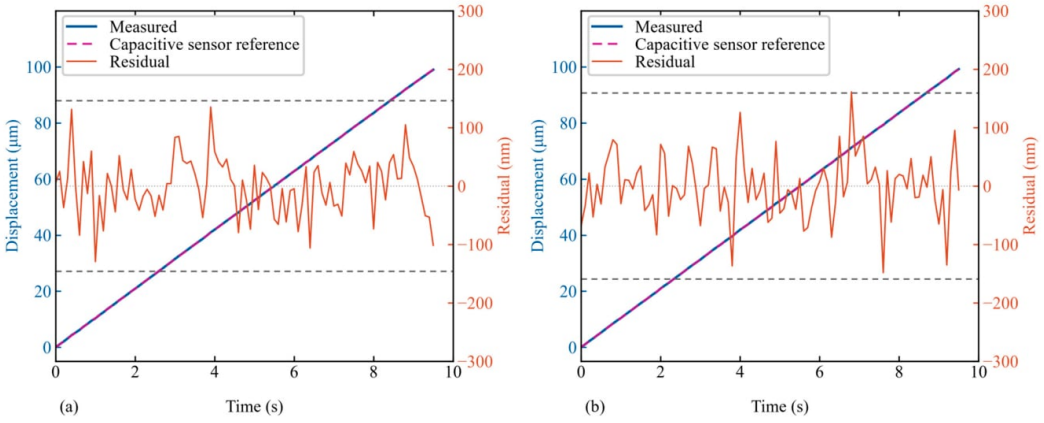

Figure 10. Linear-motion measurements over a 100 μm stroke with displacement reconstruction using two phasemeters: (**a**) *x*-axis; (**b**) *z*-axis. The blue and magenta curves show the interferometer and capacitive-sensor reference displacements, respectively. The orange curves show their differences on the right-hand vertical axes. The gray dashed lines indicate ±3σ of the residuals.

3.3.2. Repeated-Stroke Measurements

The positioning stage was driven separately along the *x*- and *z*-axes in triangular-wave motion with a nominal peak-to-peak displacement of 100 μm. Each record contained 9 one-way strokes, as shown in Figure 11. The deviation of each stroke amplitude from the capacitive-sensor reference was calculated using Equation (13). The standard deviations were 143.45 nm and 72.40 nm for the *x*- and *z*-axes, corresponding to 3σ values of 430.35 nm and 217.21 nm, respectively.

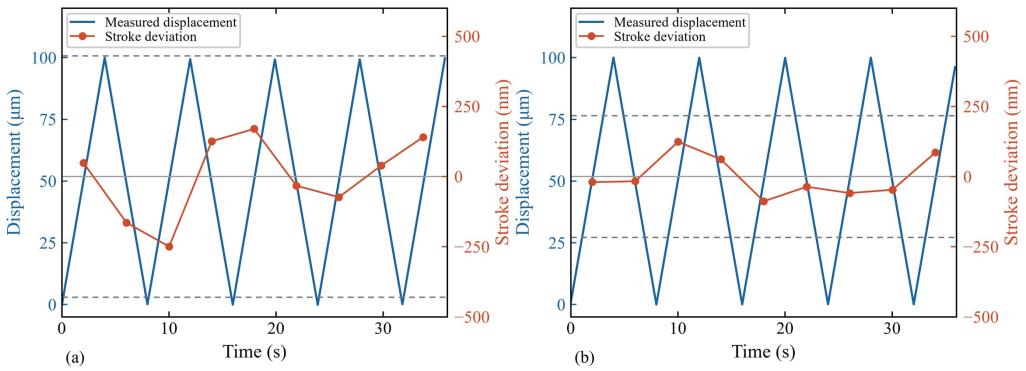

Figure 11. Repeated-stroke measurements with displacement reconstruction using two phasemeters: (**a**) *x*-axis; (**b**) *z*-axis. The blue curves show displacement on the left-hand vertical axes. The orange markers show the deviations of 9 stroke amplitudes from the capacitive-sensor reference values on the right-hand vertical axes. The gray solid and dashed lines indicate zero deviation and $\pm 3\sigma$, respectively. The 3σ values are 430.35 nm and 217.21 nm for the *x*- and *z*-axes, respectively.

3.3.3. Short-Term Stability

After the interferometer had stabilized, the positioning stage was held stationary, and a 10 s displacement record was selected for each axis. Figure 12 shows the displacement fluctuations reconstructed using two phasemeters. The standard deviations were 2.02 nm and 2.70 nm for the *x*- and *z*-axes, corresponding to 3σ values of 6.06 nm and 8.10 nm, respectively. These values characterize the short-term stability of the measurement system within the selected stationary windows. Table 3 summarizes the results obtained using two phasemeters.

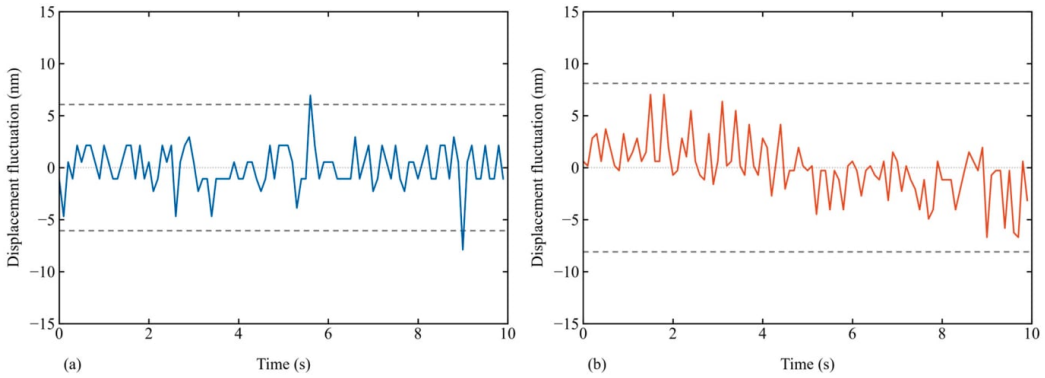

Figure 12. Displacement fluctuations within 10 s stationary windows with displacement reconstruction using two phasemeters: (**a**) *x*-axis; (**b**) *z*-axis. The gray dashed lines indicate $\pm 3\sigma$. The 3σ values are 6.06 nm and 8.10 nm for the *x*- and *z*-axes, respectively. Displacement was recorded at 10 Hz without digital filtering.

Table 3. Experimental results of displacement reconstruction using two phasemeters.

Metric	*x*-Axis (nm)	*z*-Axis (nm)
Linear-motion residual, 3σ	146.20	159.35
Maximum absolute linear-motion residual	135.30	161.05
Stroke deviation, 3σ	430.35	217.21
Stationary displacement fluctuation, 3σ	6.06	8.10

3.4. Error Mechanisms and Interpretation of the Results

Residual offsets, amplitude imbalance, and quadrature errors produce phase-dependent errors in homodyne demodulation [13,16,17,33]. To analyze their effects, the normalized signals are written as $C = \cos\varphi + \varepsilon_c$ and $S = (1 + g)\sin(\varphi + q) + \varepsilon_s$, where ε_c and ε_s are residual offsets, g is the relative amplitude mismatch, and q is the quadrature error in radians. A first-order expansion of atan2(S, C) gives

$$\delta\varphi \approx \varepsilon_s \cos\varphi - \varepsilon_c \sin\varphi + \frac{g}{2}\sin(2\varphi) + \frac{q}{2}[1 + \cos(2\varphi)]. \quad (14)$$

The offset terms produce fundamental-harmonic phase errors, whereas amplitude mismatch and quadrature errors introduce second-harmonic terms. Beam clipping, unequal optical powers, deviations from the ideal retardance, and reduced beam overlap can therefore affect the displacement results through the same phase-demodulation mechanism. Light leakage between adjacent diffraction channels introduces additional phase-dependent components and may couple the two displacement estimates.

Substituting the phase errors $\delta\varphi_{+1}$ and $\delta\varphi_{-1}$ into the displacement reconstruction equations gives

$$\delta x_{\text{phase}} = \frac{d}{4\pi}(\delta\varphi_{+1} - \delta\varphi_{-1}); \delta z_{\text{phase}} = \frac{d\tan(\theta_{\text{Lit}})}{4\pi}(\delta\varphi_{+1} + \delta\varphi_{-1}). \quad (15)$$

Common-mode phase errors primarily enter the z-axis estimate, whereas differential phase errors enter the x-axis estimate. Thus, even though the two axes share the same detection module, optical power balance and polarization alignment affect the two reconstructed displacement components differently.

The grating is mounted above the motion platform, creating an offset between the grating measurement point and the capacitive-sensor sensing location. A small parasitic rotation $\delta\Omega$ of the flexure-guided positioning stage produces a displacement change $\delta\Omega \times \ell$ at the grating, where ℓ is the vector between the two measurement points. The corresponding Abbe error along measurement direction j is

$$e_{\text{Abbe},j} \approx [\delta\Omega \times \ell]_j; \quad \left|e_{\text{Abbe},j}\right| \approx \ell_{\text{eff}}\left|\delta\theta\right|; \quad (16)$$

where ℓ_{eff} is the effective Abbe offset and $\delta\theta$ is the small angular change in the relevant direction. The elevated grating mount increases the sensitivity of the system to parasitic angular motion during translation and reversal. This mechanism may increase the motion residuals and repeated-stroke deviations, whereas stationary records do not include flexure motion driven by motion commands. The motion-comparison results also contain fluctuations in the capacitive-sensor reference. The stationary interferometer records contain the combined effects of optical and electronic noise, stage motion, and environmental fluctuations. Differences in the observed dispersion reflect these mechanical and temporal conditions.

4. Discussion

4.1. NPBS Beam Separation and Incident-Height Tolerance

The incident height at the NPBS determines the separation of the two parallel output beams and their alignment with the QPD quadrants. For the geometry in Figure 13a, the NPBS side length is $L_{\text{NPBS}} = 15$ mm, and the distances from the splitting point to the two ends of the splitting interface satisfy $L_1 + L_2 = \sqrt{2}L_{\text{NPBS}}$. With an incidence angle of $\theta_1 = 45°$, the ray geometry gives

$$s_1 = \sqrt{2}L_{\text{NPBS}}(1 - \tan\ \theta_2) - 2h, \quad (17)$$

where h is the perpendicular distance from the incident beam center to the splitting interface, and θ_2 is the refraction angle relative to the entrance-face normal. Taking the refractive

indices of air and the prism as 1 and 1.515, respectively, Snell's law gives $\theta_2 = 27.823°$. Equation (17) then becomes $s_1 = 10.018\ \text{mm} - 2h$; a nominal separation of 5 mm therefore corresponds to $h_0 = 2.509$ mm. With the prism dimensions, refractive index, and incident direction fixed, an incident-height deviation $\Delta h = h - h_0$ changes the beam separation according to

$$\Delta s_1 = -2\Delta h. \tag{18}$$

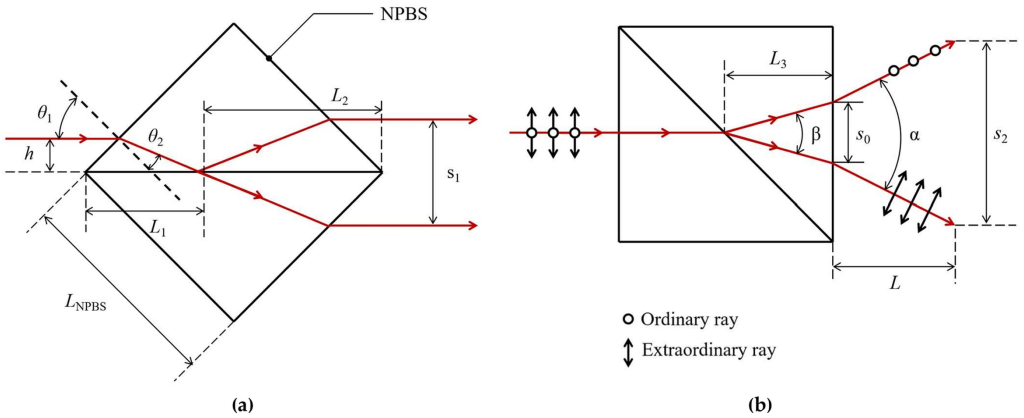

Figure 13. Geometries used in the beam-separation and assembly tolerance analysis: (**a**) NPBS geometry, showing the incidence and refraction angles θ_1 and θ_2, prism side length L_{NPBS}, splitting-point distances L_1 and L_2, incident height h, and output separation s_1; (**b**) WP–QPD geometry, showing the internal and external separation angles β and α, internal propagation distance L_3, WP–QPD axial distance L, exit-face separation s_0, and detector-plane separation s_2.

The beam waist diameter is $D_b = 2.1$ mm, which is taken as the nominal beam diameter in this geometric tolerance analysis under the near-collimated approximation. The corresponding beam radius is $r = 1.05$ mm. For a QPD active-area width of $A = 10$ mm and an interquadrant gap of $g_Q = 0.03$ mm, the nominal beam footprint remains within its assigned quadrant when

$$\frac{g_Q}{2} + r \le \frac{s_1}{2} \le \frac{10\ \text{mm}}{2} - r. \tag{19}$$

This condition gives $2.13\ \text{mm} \le s_1 \le 7.90$ mm. Substitution into Equation (17) yields the allowable incident-height deviation

$$-1.450\ \text{mm} \le \Delta h \le 1.435\ \text{mm}. \tag{20}$$

4.2. WP–QPD Spacing and Assembly Tolerance

The axial distance between the WP and the QPD controls beam separation along the orthogonal detector direction. The WP10P drawing gives a reference axial dimension of 11.5 mm, corresponding to a distance of $L_3 = 5.75$ mm from the central splitting point to the exit face. In the geometry shown in Figure 13b, the optic axis of the first calcite prism is perpendicular to the splitting plane, whereas that of the second lies in the splitting plane and is perpendicular to the incident direction. The dispersion equations [36] give principal refractive indices of $n_o = 1.64947$ and $n_e = 1.48218$ at 780 nm.

For the illustrated 45° internal interface, the ray deflection angles in the second prism after the splitting interface are $\delta_o = 5.5509°$ and $\delta_e = 5.4993°$, giving an internal beam separation angle of $\beta = \delta_o + \delta_e \approx 11.05°$. After refraction into air, the deflection angles are $\alpha_o = 9.1810°$ and $\alpha_e = 10.1208°$, with a total separation angle of $\alpha = \alpha_o + \alpha_e \approx 19.30°$.

Denoting the axial distance from the WP exit face to the QPD photosensitive surface by L, the beam-center separation is

$$s_2 = L_3(\tan\delta_o + \tan\delta_e) + L(\tan\alpha_o + \tan\alpha_e). \quad (21)$$

The first term represents the exit-face separation, $s_0 \approx 1.1124$ mm. Substituting the calculated angles gives

$$s_2 \approx 1.1124\ \text{mm} + 0.34013L. \quad (22)$$

A nominal detector-plane separation of 5 mm therefore requires $L_0 \approx 11.43$ mm. An axial displacement $\Delta L = L - L_0$ changes the separation by $\Delta s_2 \approx 0.34013\Delta L$. For the nominal beam diameter $D_b = 2.1$ mm, the projected half-width of each beam footprint along the splitting direction is

$$r_i = \frac{D_b}{2\cos\alpha_i};\quad r_o \approx 1.0636\ \text{mm};\quad r_e \approx 1.0666\ \text{mm}; \quad (23)$$

where the index i denotes the ordinary or extraordinary ray. With the beam array centered on the QPD at the nominal axial position and the detector's lateral position held fixed, the distances from the two beam centers to the quadrant boundary are 2.5 mm + $\Delta L\tan\alpha_i$. Each beam must therefore satisfy

$$\frac{g_Q}{2} + r_i \le 2.5\ \text{mm} + \Delta L\tan\alpha_i \le \frac{A}{2} - r_i. \quad (24)$$

Using the detector dimensions defined in Section 4.1, the intersection of the two ray constraints gives

$$-7.946\ \text{mm} \le \Delta L \le 8.030\ \text{mm};\quad 3.484\ \text{mm} \le L \le 19.460\ \text{mm}. \quad (25)$$

5. Conclusions

A compact dual-axis homodyne grating interferometer incorporating a WP–QPD integrated detection module was developed. By rotating the upstream non-polarizing beam splitter by 45° about the incident optical axis, the spatial arrangement of the two parallel beams was adjusted so that the four output spots were centered on the respective detector quadrants. This arrangement enables spatial matching between the dual-axis interferometric optical system and the integrated detection module. The displacement equations were derived under symmetric Littrow incidence to relate the two interferometric phases to the in-plane and out-of-plane displacement components. A prototype reading head measuring 49.2 mm × 72.5 mm × 35 mm was constructed to implement and evaluate the proposed configuration. Single-phasemeter separate-axis experiments demonstrated displacement measurement over a 100 μm stroke along both the x- and z-axes. The 3σ values of the displacement residuals relative to the capacitive-sensor reference were 184.27 nm and 157.81 nm along the x- and z-axes, respectively. With two phasemeters, 100 μm motions were applied separately along the x- and z-axes while both phases were acquired in each experiment. The corresponding residual 3σ values were 146.20 nm and 159.35 nm, the stroke-deviation 3σ values were 430.35 nm and 217.21 nm, and the 3σ values of stationary displacement fluctuations over 10 s were 6.06 nm and 8.10 nm, respectively. The single-phasemeter separate-axis experiments and displacement reconstruction using two phasemeters demonstrate the displacement measurement capability of the WP–QPD integrated detection module with both readout configurations. The spatial matching and phase-error analyses relate the detector layout, channel balance, and measurement-point alignment to displacement measurement performance.

Author Contributions: Conceptualization, D.C.; Methodology, D.C.; Software, D.S.; Validation, D.C.; Formal analysis, D.S.; Investigation, D.S. and D.C.; Resources, D.C. and J.T.; Data curation, D.S.; Writing—original draft, D.S.; Writing—review and editing, D.C.; Visualization, D.S.; Supervision, D.C.; Project administration, J.T.; Funding acquisition, D.C. All authors have read and agreed to the published version of the manuscript.

Funding: This research was funded by the Key Research and Development Program of Heilongjiang Province (2024ZXDXA27) and the National Natural Science Foundation of China (52305571).

Data Availability Statement: The raw data supporting the conclusions of this article will be made available by the authors on request.

Conflicts of Interest: The authors declare no conflicts of interest.

References

1. Gao, W.; Kim, S.W.; Bosse, H.; Haitjema, H.; Chen, Y.L.; Lu, X.D.; Knapp, W.; Weckenmann, A.; Estler, W.T.; Kunzmann, H. Measurement technologies for precision positioning. *CIRP Ann.* **2015**, *64*, 773–796. [CrossRef]
2. Gao, W.; Ibaraki, S.; Donmez, M.A.; Kono, D.; Mayer, J.R.R.; Chen, Y.-L.; Szipka, K.; Archenti, A.; Linares, J.-M.; Suzuki, N. Machine tool calibration: Measurement, modeling, and compensation of machine tool errors. *Int. J. Mach. Tools Manuf.* **2023**, *187*, 104017. [CrossRef]
3. Munnig Schmidt, R.-H. Ultra-precision engineering in lithographic exposure equipment for the semiconductor industry. *Philos. Trans. R. Soc. A* **2012**, *370*, 3950–3972. [CrossRef] [PubMed]
4. Fan, K.-C.; Wang, H.-Y.; Yang, H.-W.; Chen, L.-M. Techniques of multi-degree-of-freedom measurement on the linear motion errors of precision machines. *Adv. Opt. Technol.* **2014**, *3*, 375–386. [CrossRef]
5. Kim, J.-A.; Kim, K.-C.; Bae, E.W.; Kim, S.; Kwak, Y.K. Six-degree-of-freedom displacement measurement system using a diffraction grating. *Rev. Sci. Instrum.* **2000**, *71*, 3214–3219. [CrossRef]
6. Li, X.; Gao, W.; Muto, H.; Shimizu, Y.; Ito, S.; Dian, S. A six-degree-of-freedom surface encoder for precision positioning of a planar motion stage. *Precis. Eng.* **2013**, *37*, 771–781. [CrossRef]
7. Yu, H.; Chen, X.; Liu, C.; Cai, G.; Wang, W. A survey on the grating based optical position encoder. *Opt. Laser Technol.* **2021**, *143*, 107352. [CrossRef]
8. Cui, C.; Li, X.; Wang, X. Grating interferometer: The dominant positioning strategy in atomic and close-to-atomic scale manufacturing. *J. Manuf. Syst.* **2025**, *82*, 1227–1251. [CrossRef]
9. Heilmann, R.K.; Chen, C.G.; Konkola, P.T.; Schattenburg, M.L. Dimensional metrology for nanometer-scale science and engineering: Towards sub-nanometer accurate encoders. *Nanotechnology* **2004**, *15*, S504–S511. [CrossRef]
10. Hu, P.-C.; Chang, D.; Tan, J.-B.; Yang, R.-T.; Yang, H.-X.; Fu, H.-J. Displacement measuring grating interferometer: A review. *Front. Inf. Technol. Electron. Eng.* **2019**, *20*, 631–654. [CrossRef]
11. Teimel, A. Technology and applications of grating interferometers in high-precision measurement. *Precis. Eng.* **1992**, *14*, 147–154. [CrossRef]
12. Kunzmann, H.; Pfeifer, T.; Flügge, J. Scales vs. laser interferometers performance and comparison of two measuring systems. *CIRP Ann.* **1993**, *42*, 753–767. [CrossRef]
13. Lin, D.; Jiang, H.; Yin, C. Analysis of nonlinearity in a high-resolution grating interferometer. *Opt. Laser Technol.* **2000**, *32*, 95–99. [CrossRef]
14. Huang, Y.; Chang, D.; Mao, Y.; Zhang, Y.; Hu, S.; Qu, C.; Zhang, M.; Tan, J.; Fan, Z. Real-time compensation for signal loss in homodyne interferometry: A CORDIC-based programmable gain control solution. *Meas. Sci. Technol.* **2026**, *37*, 306106. [CrossRef]
15. Shin, D.; Kim, B. A laser interferometer encoder with two micromachined gratings generating phase-shifted quadrature. *J. Micromech. Microeng.* **2011**, *21*, 085036. [CrossRef]
16. Heydemann, P.L.M. Determination and correction of quadrature fringe measurement errors in interferometers. *Appl. Opt.* **1981**, *20*, 3382–3384. [CrossRef] [PubMed]
17. Hu, P.; Zhu, J.; Guo, X.; Tan, J. Compensation for the variable cyclic error in homodyne laser interferometers. *Sensors* **2015**, *15*, 3090–3106. [CrossRef] [PubMed]
18. Watchi, J.; Cooper, S.; Ding, B.; Mow-Lowry, C.M.; Collette, C. Contributed Review: A review of compact interferometers. *Rev. Sci. Instrum.* **2018**, *89*, 121501. [CrossRef] [PubMed]
19. Gao, W.; Kimura, A. A three-axis displacement sensor with nanometric resolution. *CIRP Ann.* **2007**, *56*, 529–532. [CrossRef]
20. Kimura, A.; Gao, W.; Kim, W.J.; Hosono, K.; Shimizu, Y.; Shi, L.; Zeng, L. A sub-nanometric three-axis surface encoder with short-period planar gratings for stage motion measurement. *Precis. Eng.* **2012**, *36*, 576–585. [CrossRef]

21. Lin, J.; Guan, J.; Wen, F.; Tan, J. High-resolution and wide range displacement measurement based on planar grating. *Opt. Commun.* **2017**, *404*, 132–138. [CrossRef]
22. Shimizu, Y.; Ito, T.; Li, X.; Kim, W.; Gao, W. Design and testing of a four-probe optical sensor head for three-axis surface encoder with a mosaic scale grating. *Meas. Sci. Technol.* **2014**, *25*, 094002. [CrossRef]
23. Li, X.; Shi, Y.; Xiao, X.; Zhou, Q.; Wu, G.; Lu, H.; Ni, K. Design and testing of a compact optical prism module for multi-degree-of-freedom grating interferometry application. *Appl. Sci.* **2018**, *8*, 2495. [CrossRef]
24. Kimura, A.; Gao, W.; Zeng, L. Position and out-of-straightness measurement of a precision linear air-bearing stage by using a two-degree-of-freedom linear encoder. *Meas. Sci. Technol.* **2010**, *21*, 054005. [CrossRef]
25. Liu, C.-H.; Cheng, C.-H. Development of a grating based multi-degree-of-freedom laser linear encoder using diffracted light. *Sens. Actuators A Phys.* **2012**, *181*, 87–93. [CrossRef]
26. Cheng, F.; Fan, K.-C. Linear diffraction grating interferometer with high alignment tolerance and high accuracy. *Appl. Opt.* **2011**, *50*, 4550–4556. [CrossRef] [PubMed]
27. Kimura, A.; Gao, W.; Arai, Y.; Zeng, L. Design and construction of a two-degree-of-freedom linear encoder for nanometric measurement of stage position and straightness. *Precis. Eng.* **2010**, *34*, 145–155. [CrossRef]
28. Guan, J.; Köchert, P.; Weichert, C.; Tutsch, R. A high performance one-dimensional homodyne encoder and the proof of principle of a novel two-dimensional homodyne encoder. *Precis. Eng.* **2013**, *37*, 865–870. [CrossRef]
29. Lv, Q.; Liu, Z.; Wang, W.; Li, X.; Li, S.; Song, Y.; Yu, H.; Bayanheshig; Li, W. Simple and compact grating-based heterodyne interferometer with the Littrow configuration for high-accuracy and long-range measurement of two-dimensional displacement. *Appl. Opt.* **2018**, *57*, 9455–9463. [CrossRef] [PubMed]
30. Chang, D.; Yin, Z.; Sun, Y.; Hu, P.; Tan, J.; Fan, Z. Spatially separated heterodyne grating interferometer for in-plane and out-of-plane displacement measurements. *Photonics* **2022**, *9*, 830. [CrossRef]
31. Cui, C.; Gao, L.; Zhao, P.; Yang, M.; Liu, L.; Ma, Y.; Huang, G.; Wang, S.; Luo, L.; Li, X. Towards multi-dimensional atomic-level measurement: Integrated heterodyne grating interferometer with zero dead-zone. *Light Adv. Manuf.* **2025**, *6*, 40. [CrossRef]
32. Lu, Z.; Wei, P.; Wang, C.; Jing, J.; Tan, J.; Zhao, X. Two-degree-of-freedom displacement measurement system based on double diffraction gratings. *Meas. Sci. Technol.* **2016**, *27*, 074012. [CrossRef]
33. Hu, P.; Zhu, J.; Zhai, X.; Tan, J. DC-offset-free homodyne interferometer and its nonlinearity compensation. *Opt. Express* **2015**, *23*, 8399–8408. [CrossRef] [PubMed]
34. Hsieh, H.-L.; Chen, W. Heterodyne Wollaston laser encoder for measurement of in-plane displacement. *Opt. Express* **2016**, *24*, 8693–8707. [CrossRef] [PubMed]
35. Reyes, A.K.; Rodríguez-Zurita, G.; Montes-Pérez, A.; Sánchez-Aguilar, J.R.; García-Lechuga, L.; Toto-Arellano, N.-I. Development of a Wollaston phase grating polarized interferometer for simultaneous generation of interferograms. *Opt. Lasers Eng.* **2025**, *186*, 108739. [CrossRef]
36. Ghosh, G. Dispersion-equation coefficients for the refractive index and birefringence of calcite and quartz crystals. *Opt. Commun.* **1999**, *163*, 95–102. [CrossRef]

Disclaimer/Publisher's Note: The statements, opinions and data contained in all publications are solely those of the individual author(s) and contributor(s) and not of MDPI and/or the editor(s). MDPI and/or the editor(s) disclaim responsibility for any injury to people or property resulting from any ideas, methods, instructions or products referred to in the content.